Helical Striations and Magnetic Flux Compression in an Axially Premagnetized Gas-Puff z-Pinch Imploding Onto a Dense Central Target

Joe M. Chen, *Member, IEEE*, George V. Dowhan, *Member, IEEE*, Brendan J. Sporer, David A. Yager-Elorriaga, *Member, IEEE*, Nicholas M. Jordan, *Senior Member, IEEE*, and Ryan D. McBride, *Member, IEEE*

***Abstract*— Presented is a platform for studying instability development and magnetic flux compression in a low-density plasma as the plasma implodes onto a dense cylindrical target. This platform, developed for the MAIZE pulsed power facility at the University of Michigan, utilizes the plasma from an annular gas-puff z-pinch to compress a preapplied axial magnetic field onto a central cylindrical rod. For the experiments presented, MAIZE supplied a driving current pulse that rose from 0 to 500 kA in approximately 150 ns. Images captured with fast framing cameras show that steep helical striations formed in the low-density plasma when the axial field (0.25–0.75 T) was applied. Measurements of the axial field during the implosion indicate a magnetic flux compression efficiency of nearly 50% (relative to an ideal flux compression model where an imploding thin shell with zero resistivity is assumed). The experiments presented are relevant to the magnetized liner inertial fusion (MagLIF) program on the *Z* facility at Sandia National Laboratories, where low-density plasma in the facility's power feed is likely compressed onto the outer surface of the dense MagLIF liner, potentially seeding instability structure in the liner.**

***Index Terms*— Gas-puff, inertial confinement fusion (ICF), instability, magnetic flux compression, magnetized liner inertial fusion (MagLIF), magneto-inertial fusion (MIF), plasma, pulsed power, z-pinch.**

I. Introduction

FAST z-pinch implosions are subject to instabilities, such as the acceleration-driven magneto-Rayleigh–Taylor (MRT) instability (MRTI), $m = 0$ sausage instability, $m = 1$ kink instability, and $m \geq 1$ helical instabilities in general, where m is the azimuthal mode number [1], [2], [3], [4], [5], [6], [7], [8], [9]. A fast z-pinch configuration where these instabilities are relevant is the magnetized liner inertial fusion (MagLIF) concept on the Z pulsed power facility at Sandia National Laboratories [10], [11], [12], [13], [14].

A MagLIF target consists of a hollow cylindrical shell (liner) filled with deuterium fusion fuel. The liner is usually made of a low-atomic-number metal such as beryllium. The fuel is preheated with a laser and premagnetized with an axial magnetic field. The target is compressed radially by the $\mathbf{J} \times \mathbf{B}$ force density that results from the 20-MA, 100-ns current pulse supplied by the Z facility. This magnetic drive implodes the liner, compressing the fuel to thermonuclear conditions. As the liner accelerates to the axis, its outer surface is susceptible to MRTI as well as sausage, kink, and helical instabilities. These instabilities can feed through the liner wall, degrading the uniformity and confinement of the assembled fuel.

A key component of the MagLIF concept is the applied axial magnetic field (∼10–30 T). This field is pre-embedded within the entire load volume prior to the implosion. It is generated from a large external Helmholtz-like coil pair that surrounds the load region and is pulsed over a long time scale (∼3 ms) [15]. The long time scale allows the axial field to diffuse into the liner, fuel, and surrounding metallic electrodes prior to the liner implosion. During the fast (∼100 ns) liner implosion, the axial magnetic field cannot diffuse out of the preheated fuel or through the liner wall, and thus the magnetic flux is trapped inside the fuel and is largely conserved throughout the implosion. The resulting flux compression process amplifies the magnetic field strength in the fuel to >1000 T by the time of stagnation. Throughout the implosion, the axial field reduces thermal conduction losses from the hot fuel to the cold liner wall. During fusion burn (at stagnation), the axial field traps charged fusion products within the fuel for self-heating.

Penetrating radiography experiments on the Z facility have shown that the applied axial field modifies the instability structure in imploding MagLIF liners. With no axial field applied, the instability structure is azimuthally symmetric ($m = 0$) [16], [17]. With a 10-T axial field applied, the instability structure is helical, with pitch angles of approximately 30° and $m \approx 6$ at a fuel convergence ratio of ≈7 [18], [19]. These helical structures likely feed through to the fuel by the time of stagnation [11]. We note that helical instabilities are

Manuscript received 30 November 2023; revised 16 May 2024; accepted 25 July 2024. This work was supported in part by Sandia's Laboratory Directed Research and Development Program under Project 226066 and in part by the National Nuclear Security Administration's (NNSA) Stewardship Science Academic Alliances Program under DOE Cooperative Agreement DE-NA0004148. The review of this article was arranged by Senior Editor F. Beg. *(Corresponding author: Joe M. Chen.)*

Joe M. Chen, George V. Dowhan, Nicholas M. Jordan, and Ryan D. McBride are with the Department of Nuclear Engineering and Radiological Sciences, University of Michigan, Ann Arbor, MI 48109 USA (e-mail: joech@umich.edu).

Brendan J. Sporer was with the Department of Nuclear Engineering and Radiological Sciences, University of Michigan, Ann Arbor, MI 48109 USA. He is now with TAE Technologies, Foothill Ranch, CA 92610 USA.

David A. Yager-Elorriaga is with Sandia National Laboratories, Albuquerque, NM 87123 USA.

Color versions of one or more figures in this article are available at https://doi.org/10.1109/TPS.2024.3435720.

Digital Object Identifier 10.1109/TPS.2024.3435720

also present in other z-pinch configurations, including gas-puff z-pinches [20], [21] and nonimploding metal liners [9], [22], [23], [24].

There have been a few hypotheses developed to explain the large helical pitch angles observed in MagLIF liner implosions. One hypothesis involves the electrothermal instability (ETI) [25], which is due to nonuniform resistive heating along the surface of the liner seeding an initial perturbation prior to the liner implosion. A second hypothesis involves the Hall interchange instability (HII), which develops in the low-density coronal plasma that surrounds the liner early in the current pulse [26], [27]. The HII enables magnetic-field-aligned (force-free) currents to flow, which can induce helical striations that can imprint on the outer surface of the dense liner material. A third hypothesis [28] involves magnetic flux compression occurring in low-density plasma that surrounds the liner and is supplied by the Z facility's magnetically insulated transmission lines (MITLs). The MITLs deliver power (electrical current and magnetic pressure) to the imploding MagLIF liner. Early in the power pulse, this low-density plasma (and the preapplied axial magnetic field embedded within it) is swept up by the implosion-driving magnetic pressure and compressed onto the liner's outer surface. Any instability structure contained in the magnetized low-density plasma can then imprint, potentially through current density perturbations, onto the liner's dense outer surface. We note that the dominant mechanism responsible for the observed helical instabilities in MagLIF liner implosions is still uncertain. We further note that some combination of the above three processes may also be possible.

This article explores the third hypothesis mentioned in the preceding paragraph, which involves magnetic flux compression in a surrounding low-density plasma [28]. On the Z facility, the high current densities and high field stresses can cause the desorption of contaminant particles and the explosive emission of charged particles from electrode surfaces [29]. As the current density increases, the emission and desorption processes result in a flowing low-density surface plasma. In the MITL section close to the load region, the plasma is largely confined to the electrode surfaces via the magnetic pressure of the driving current pulse. However, issues can arise when this plasma flows into and fills the load region. This can cause unknown effects which may be detrimental to the experiment. For example, this low-density plasma can conduct current across the anode–cathode (AK) gap, thus reducing the current and magnetic drive pressure delivered to the liner target. Recent simulations have shown that by 60 ns into the current pulse, the MITL immediately surrounding the liner target is filled with low-density plasma, with an electron number density of $n_e \lesssim 10^{17}$ cm^{-3} [29].

The experiments presented in this article were performed on the MAIZE pulsed power facility at the University of Michigan [30]. For these experiments, MAIZE supplied a driving current pulse that rose from 0 to 500 kA in approximately 150 ns. At this current level, it is difficult to generate electrode plasmas from thick metal electrodes with high enough plasma densities to be observable with standard diagnostic techniques. Thus, stripline platforms using thin-foil electrodes backed by solid 3-D printed insulating material have been developed to study electrode plasma formation on MAIZE [31]. However, even with such a platform, it is still difficult to both generate and sweep this plasma onto an imploding liner. Because of this, we developed a new platform—one which utilizes MAIZE's annular gas-puff z-pinch system with $n_e \sim 10^{17}$–10^{18} cm^{-3} [32], [33] to emulate the low-density plasma expected to be presented in the MITLs on the Z facility. Using this system, we can experimentally investigate instability development and magnetic flux compression of a pre-embedded axial magnetic field as the low-density plasma from the gas-puff z-pinch implodes onto a solid cylindrical target.

The results presented in this article include experimental observations of helical striations with large pitch angles in the low-density plasma when a pre-embedded axial magnetic field of $|B_{z0}| = 0.25$–0.75 T (at $z = 10$ mm) is applied. Observation shows that the polarity of the applied axial field determines the direction of the helical striations (i.e., the "handedness" of the striations). It also shows that the magnitude of the pitch angle grows as the strength of the axial field increases. Schlieren imaging shows that at higher axial field strengths, shorter wavelength perturbations are partially stabilized and only longer wavelength perturbations persist. Measurement of the gas-puff implosion trajectory onto the central rod is shown to occur around the time of peak current, with a compressed plasma sheath thickness of approximately 1 mm. Measurement of the flux compression efficiency is found to be nearly 50%, relative to an ideal flux compression model where an imploding thin shell with zero resistivity is assumed.

Regarding various hypotheses for the large helical pitch angles observed in MagLIF liner implosions, it is important to note that the experiments presented herein do not attempt to isolate the flux compression mechanism from the other proposed mechanisms. For example, HII could also be present in our system, since both HII and flux compression are expected to occur in the low-density plasmas surrounding the central metal liner [26], [27]. Furthermore, the experiments reported herein focus solely on the evolution of the low-density plasma as it implodes onto the central rod while ignoring the ETI effects that may be occurring in the rod. In future experiments, the solid central rod will be replaced with an imploding liner made from thin aluminum foil [34]. The goal of this modified platform will be to observe the instability coupling (seeding) that results from the low-density gas-puff plasma imploding onto the later-imploding thin-foil liner. Together with advanced 3-D Hall-magnetohydrodynamics (MHD) simulations, such experiments might be able to determine which mechanisms are dominant in seeding the subsequent liner implosion instabilities. However, such a determination would be quite challenging and is beyond the scope of this article.

II. Experimental Configuration and Diagnostics

The MAIZE facility is comprised of 80 capacitors (each having a capacitance of 40 nF) and 40 triggered spark-gap switches. When bipolar charged to ±100 kV, MAIZE stores 16 kJ of electrical energy. The machine is a single-cavity, low-impedance (∼0.1 Ω) linear transformer driver (LTD). Because of its low impedance, the current pulse supplied by MAIZE is highly sensitive to the load impedance. For these experiments,

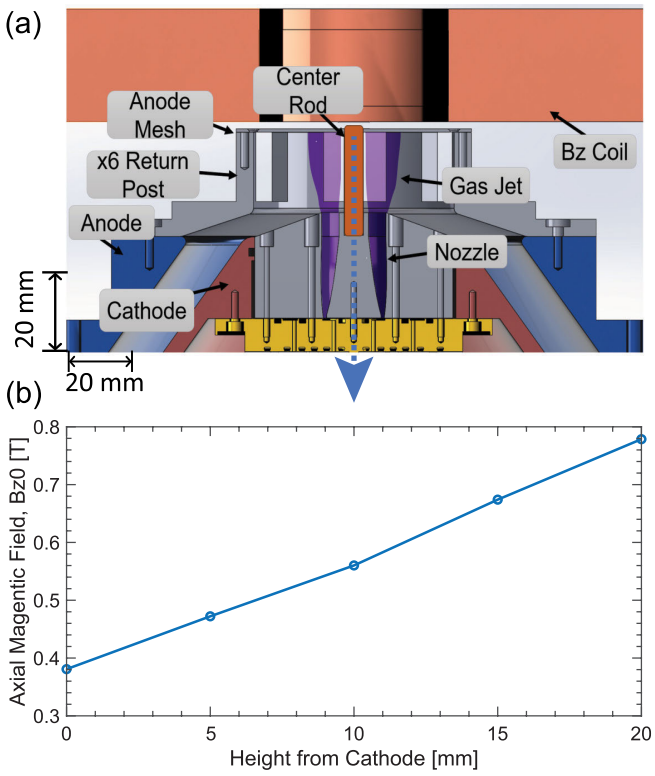

Fig. 1. (a) Cross-sectional illustration of the experimental load region. The transmission line output is shown in red (cathode) and blue (anode). The gas-puff injection system is inserted into the cathode (bottom) side of the AK gap and is shorted to the anode through a central rod. The gas jet marked in purple is ejected upward from the nozzle, fills the AK gap, and escapes the AK gap through the anode mesh at the top of the gap. The gas continues upward through the central bore of the axial magnetic field (B_z) coil. The coil itself sits above the anode mesh and provides a fringed axial magnetic field to the entire load region. (b) Plot of the axial magnetic field strength as a function of height. Here, $z = 0$ mm is the cathode height, while $z = 20$ mm is the height of the anode mesh. The values plotted for each height are the values found on axis, at $r = 0$. Their measurement locations correspond to the blue dashed line in (a).

the initial load inductance was 6.4 nH, while the final load inductance was 11.7 nH (i.e., $\Delta L = 5.3$ nH). Additionally, the charge voltage was ± 70 kV. These conditions resulted in a nominal peak current of around 500 kA and a current rise time of approximately 150 ns.

The experimental load region is illustrated in Fig. 1. It consisted of a single annular gas puff (supplied by a fast-valve coupled to a nozzle), a center rod, an exit mesh, and six return-current posts. The original gas-puff system [32], [33] allows for two independent annular gas shells from two independent nozzles. Since MAIZE is sensitive to high inductance, the nozzles themselves can become problematic, as they provide additional inductive paths for the current to follow when there is no gas present in the nozzles. To reduce the inductance of this hardware, the nozzle insert was redesigned to have a solid-metal-filled outer nozzle. Additionally, the radius where the six return-current posts reside was reduced down to 32 mm using an anode extension (see Fig. 1).

The gas-puff plenum was filled with -2 psig (17 μg/cm^3) of argon gas. The gas was ejected from the plenum, through the single (inner) nozzle, into the 20-mm-tall AK gap via an inductive piston. The nozzle is located on the bottom (cathode) side of the MAIZE load region. The nozzle exit has an outer radius of 10 mm and an inner radius of 4.7 mm. MAIZE is fired 700 μs after gas release to ensure that the gas has fully crossed the AK gap. An anode mesh is placed above the gas puff to allow the gas to escape on the anode side, preventing gas build-up in the AK gap.

A central rod with a radius of 3 mm was placed on axis. Most of the experiments used a copper central rod to allow compression of the axial field onto a stationary conductor that is thicker than the electrical skin depth. Measurements were also performed using a dielectric rod, which allowed the compressed field to exist inside the rod volume, all the way to the axis. The dielectric rod housed a B-dot probe to measure the compressed field strength on axis.

The load was premagnetized with an axial field using a single 80-turn magnetic field coil placed on top of the anode mesh and separated from the mesh by a thin sheet of polycarbonate. The coil was driven by an independent capacitor bank of 1.2 mF and a current rise time of 2 ms. MAIZE is discharged when the coil reaches peak current, which corresponds to the peak field strength of the coil. The long discharge time allows the axial field to diffuse uniformly through the load hardware. The magnetization uses the fringe field of the coil (the field that exists below the bottom edge of the solenoid winding). The reason for this is that the coil's inner radius does not fit around the return-current structure. The variation in the peak axial field strength as a function of height, measured using a gaussmeter, is shown in Fig. 1. It is nearly linear across the AK gap.

For these experiments, a fast 12-frame camera captured visible-light self-emission images of the imploding plasma shell. Each frame was exposed for 5 ns with an interframe time of 33 ns. Additionally, a 2-ns, 532-nm Nd:YAG laser was used to probe the plasma structure of the gas shell. The diameter of the beam was set to 5.4 mm using a beam expander. The beam expander also served as a spatial filter to improve the beam quality; this was done using a 100-μm pinhole that was co-located with the beam focal spot that existed between the two expander optics. The beam was then passed through an 80:20 beam splitter to form a reference beam and a probe beam for interferometry (the interferometry data are not presented in this article). The probe beam was then passed through the experiment vacuum chamber. On the output side of the experiment chamber, a 50:50 beam splitter was used to provide a probe beam for interferometry and a probe beam for schlieren imaging. A 4f telescope with a focal length of 750 mm and a collection angle of 3.8° was used to image the schlieren beam onto a Nikon DLSR camera. A photodiode was used to collect a timing fiducial. The schlieren system included a beam stop with a diameter of 500 μm, placed at the beam's final unperturbed focal spot. This resulted in a bright schlieren image on a dark background field (i.e., dark-field schlieren).

III. Experimental Results and Analysis

A. Implosion Trajectories

In Fig. 2(a), we present visible-light self-emission images collected from the fast 12-frame camera. These data reveal a

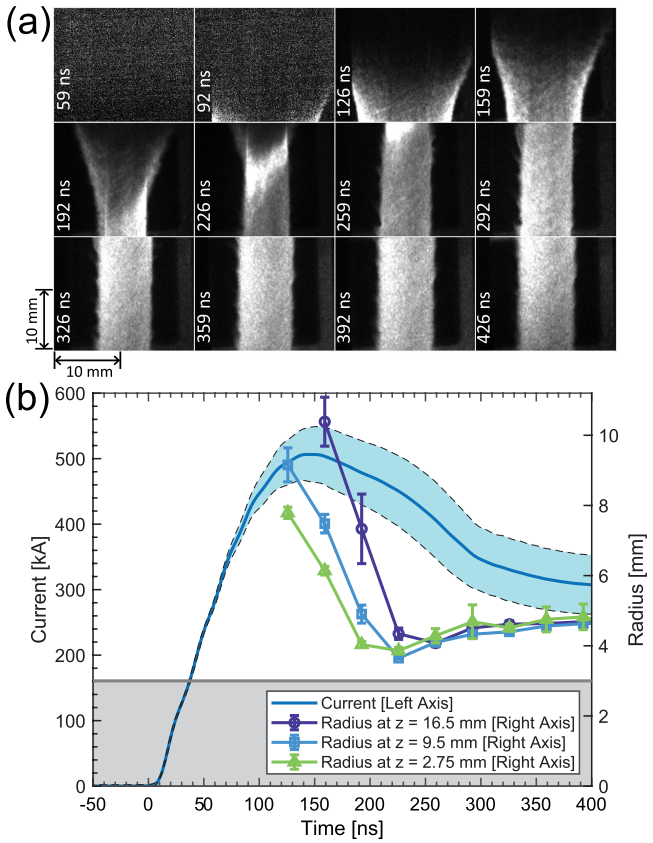

Fig. 2. (a) Representative visible-light self-emission images from an experiment with $B_{z0} = -0.75$ T at $z = 10$ mm. The field of view in each image is 21 mm × 21 mm. (b) Average drive current and its standard deviation over 17 shots, which includes shots with and without an applied B_{z0}. Also plotted are the implosion trajectories for three different axial heights: $z = 2.75$ mm (green), $z = 9.5$ mm (blue), and $z = 16.5$ mm (purple). The center rod is represented by the gray shaded area. From bottom to top, the imploding sheath impacts the rod over the time period of 194–260 ns.

conical shape to the imploding plasma sheath. This "zippering" effect is well known in the gas-puff z-pinch community and is generally undesirable [35]. In Fig. 2(a), the zippering persists until maximum compression occurs along the central rod. Note that in the first two frames of Fig. 2(a), a very dim plasma is present; these frame times correspond to a drive current of about 300–400 kA [see Fig. 2(b)].

The outer radial edge of the imploding plasma sheath is determined using an automated MATLAB script. Each image is first contrast enhanced and smoothed using a 5 pixel × 5 pixel (corresponding to 140 μm × 150 μm) median filter. The images are then binarized using a threshold intensity of 0.15 times the maximum intensity found in the image. A horizontal lineout is then taken across the binarized image to determine the outer radial edge of the plasma sheath.

In Fig. 2(b), the outer radial edge of the plasma sheath is plotted as a function of time for three different axial locations. Each radial value plotted is the average sheath radius taken over a 5-mm-tall window that is centered on the axial location indicated: $z = 2.75$ mm (green), $z = 9.5$ mm (blue), and $z = 16.5$ mm (purple). These three trajectories help quantify the differences in implosion timing of the plasma sheath from top to bottom (anode to cathode). Near 200 ns, the top of the sheath is at a radial position of $r \approx 7$ mm, the mid height is at $r \approx 5$ mm, and the bottom has already collapsed onto the central rod with a plasma outer radius of $r \approx 4$ mm. The time difference between the top and bottom of the sheath collapsing onto the rod is approximately 60 ns. At peak compression along the rod, the thickness of the plasma sheath is about 0.5 mm. The plasma sheath then decompresses back out to a thickness of about 2 mm. The sheath thickness is quite uniform axially along the surface of the rod, despite the conical shape of the imploding sheath. The full compression of the plasma occurs at about 260 ns, which is approximately 110 ns after peak current.

B. Instability Evolution and Stabilization

In Fig. 3, the outer edge of the imploding plasma sheath has been traced (blue line) using the edge-detection method described in Section III-A. For this non-premagnetized case (i.e., $B_{z0} = 0$), the dominant instability structure is azimuthally symmetric ($m = 0$). The $m = 0$ structure has been determined from the full-view images of this shot [see Fig. 6(a)], where the striations are observed to be horizontally oriented. Using the traced edges in Fig. 3, the instability amplitude is taken as the average radial distance between the peaks and the troughs. The instability wavelength is taken as the average axial distance between consecutive peaks. At $t = 197$ ns, the instability amplitude is about 0.14 ± 0.09 mm, and the wavelength is 0.9 ± 0.3 mm. As the plasma collapses onto the central rod (around $t = 230$ ns), the instability structure transitions quickly, growing to an amplitude of about 0.6 ± 0.2 mm and a wavelength of 1.6 ± 0.3 mm.

The data in Fig. 3 also reveal mode-merger events occurring during the time period of $t = 230$–297 ns, at axial positions of $z = 0$–6 mm. A mode-merger event is where two or more shorter wavelength structures merge into a single longer wavelength structure. Mode merger events have been observed previously in solid liner implosions [24]. We also note here that the plasma appears to drift in the upward ($+z$) direction (from cathode to anode). The axial velocity is taken as the change in the axial position of a given instability peak over the interframe time period. For the time period $t = 263.6$–363.6 ns, shown partially in Fig. 3, the peaks of the instability structure are well defined and give an average axial velocity of 21 ± 9 μm/ns.

In Fig. 4, we present schlieren imaging data for four different cases: $B_{z0} = 0$, $B_{z0} = +0.25$ T, $B_{z0} = +0.5$ T, and $B_{z0} = +0.75$ T (where these B_{z0} values are the fringe field values taken at $z = 10$ mm). All four images were taken around the same time of $t = 238$ ns, which is after the entire height of the plasma sheath has collapsed onto the rod. The tracked boundaries are shown in green. The instability amplitudes, A, were taken as $2\sqrt{2}\sigma$, where σ is the standard deviation in the plasma radius. Using this definition, we found $A = 1.5$, 1.6, 1.5, and 0.8 mm for $B_{z0} = 0$, $+0.25$, $+0.5$, and $+0.75$ T, respectively. The instability wavelengths in the axial direction, λ_z, were characterized in two different ways, where both ways made use of discrete Fourier transforms (DFTs). The first method used the DFT power spectra directly, taking the largest peak in each spectrum as the dominant wavelength. This gave $\lambda_z = 3.1$, 5.0, 5.0, and 6.9 mm for $B_{z0} = 0$, $+0.25$,

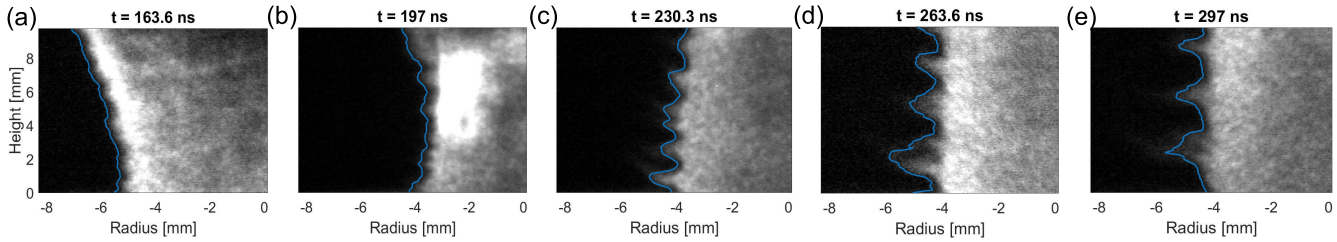

Fig. 3. Visible-light self-emission images of the $B_{z0} = 0$ experiment as the conical plasma sheath compresses onto the central rod. The plasma boundary was tracked for each image and is indicated by the blue lines. These images show a notable change in the instability amplitude past 230 ns, when the process transitions from implosion onto the rod to explosion away from the rod. These images also show the instability structures evolving from shorter wavelengths to longer wavelengths over time (i.e., the so-called "inverse cascade") due to mode merger events, and an upward axial drift in the plasma structure (in the $+z$-direction).

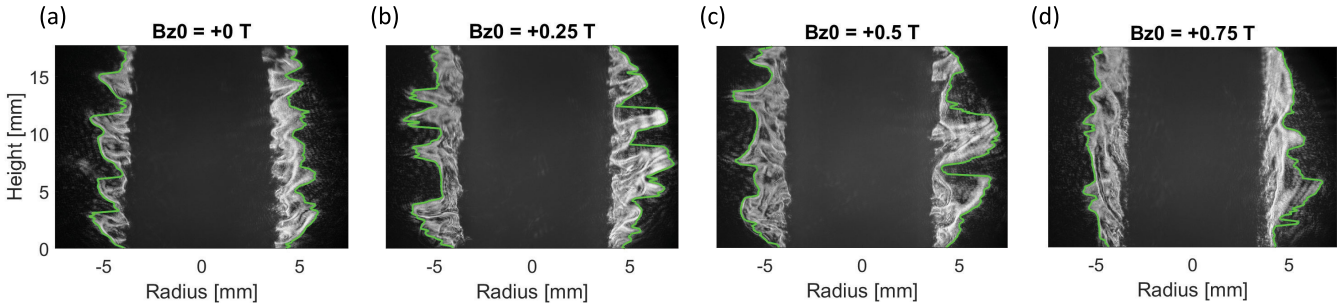

Fig. 4. Schlieren images taken after peak compression onto the rod for four cases. (a) $B_{z0} = 0$. (b) $B_{z0} = +0.25$ T. (c) $B_{z0} = +0.5$ T. (d) $B_{z0} = +0.75$ T. These B_{z0} values are for the fringe field at $z = 10$ mm. The plasma boundary was tracked for each image and is indicated by the green lines. Stabilization of shorter wavelength modes is observed as $|B_{z0}|$ is increased.

$+0.5$, and $+0.75$ T, respectively. The second method used each DFT power spectrum as an energy distribution function, which could be characterized by its mean value (mean wavelength). With this description, 50% of the total fluctuation energy is carried by wavelengths below the mean value, and 50% of the total fluctuation energy is carried by wavelengths above the mean value. Using this method, we found $\lambda_z = 4.2$, 4.5, 4.8, and 6.5 mm for $B_{z0} = 0$, $+0.25$, $+0.5$, and $+0.75$ T, respectively.

The analyses in the previous paragraph suggest that higher B_{z0} cases tend toward larger λ_z and smaller A. However, as noted in [36] and [37], images like those presented in Fig. 4 are 2-D projections of 3-D objects. The full instability amplitude is only observable by nonpenetrating imaging diagnostics in the case of an azimuthally symmetric ($m = 0$) structure. For helical structures, the spikes partially obscure the camera's view of the troughs (bubbles). This causes the observed instability amplitudes, A_{obs}, to be smaller than the true instability amplitudes, A_{true}. To quantify the obstructed view effects, a 3-D geometric model with cycloidal perturbations (sharp cusps) was developed (see Fig. 5). This model is similar to that shown in [36] and mentioned in [37]. The model presented herein (Fig. 5) consists of a cylindrical surface with a radius of 5 mm, perturbed with a single mode. Various single modes were tested, including helical pitch angles that spanned from $\phi = 0°$ (i.e., an azimuthally symmetric, $m = 0$ case) to $\phi = 50°$ (i.e., a steep helical case); $\lambda_z = 1$, 3, or 5 mm; and $A_{\text{true}} = 1$ or 2 mm, where A_{true} in this cycloidal model is the full bubble-to-spike radial distance. These parameter ranges were chosen because they are similar to those observed in the experimental data. In particular, for $\phi = 30°$ and $\lambda_z = 3$ mm, the ratio $A_{\text{obs}}/A_{\text{true}}$ is 0.92 and 0.37 for $A_{\text{true}} = 1$ and 2 mm, respectively. In principle, we could apply such corrections to our experimentally observed instability amplitudes, A. However, doing so is difficult to justify for the data presented herein, since the corrections become exceedingly large and unreliable for the large A and ϕ values presented in this study. It is even more difficult to justify given that the instability structures observed in this study are not truly cycloidal or single modes. Therefore, due to the nonpenetrating diagnostic limitations, it is difficult to quantify with certainty the degree to which the instability structures were stabilized by B_{z0} in these experiments.

C. Helical Striations

In these experiments, helical striations were observed for all cases with $B_{z0} \neq 0$. This is shown in Fig. 6, where visible-light self-emission images are presented for three cases: $B_{z0} = 0$, $B_{z0} = +0.75$ T (at $z = 10$ mm), and $B_{z0} = -0.75$ T (at $z = 10$ mm). The three frames presented in Fig. 6 were chosen because they were close to the same radius during the implosion. These data show very clearly that an applied axial field produces large helical pitch angles even when the applied axial field ($|B_{z0}| < 1$ T) is much smaller than the peak implosion-driving azimuthal field ($B_\theta \approx 30$ T). The peak azimuthal field comes from

$$B_\theta = \frac{\mu_0 I}{2\pi r}, \tag{1}$$

where $I \approx 500$ kA is the peak implosion-driving current and $r \approx 3$ mm is the minimum possible plasma radius (i.e., the rod radius).

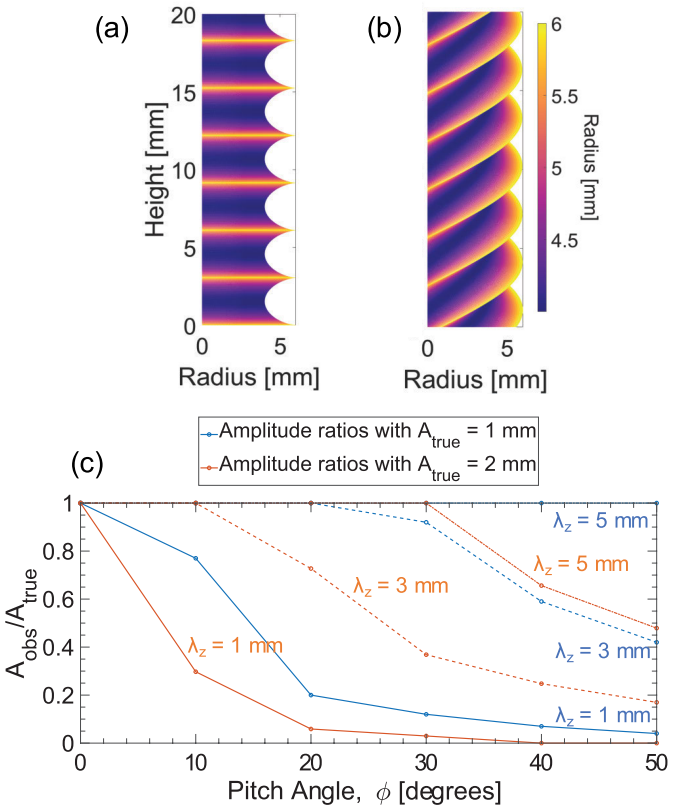

Fig. 5. Analysis of the obstructed viewing effects that occur when attempting to observe helical instability troughs side-on with nonpenetrating imaging diagnostics. (a) and (b) Two-dimensional views of 3-D models of single-mode cycloidal perturbations. The pitch angle in (a) is $\phi = 0°$ (i.e., an azimuthally symmetric, $m = 0$ case), while in (b) it is $\phi = 30°$ (i.e., a steep helical case). In both cases, the true bubble-to-spike amplitude is 2 mm and the axial wavelength is 3 mm; however, in the helical case, the observed amplitude trough is not nearly as deep as in the $m = 0$ case, which shows the true depth of the perturbation. (c) Ratio of the observed instability amplitude (A_{obs}) to the true instability amplitude (A_{true}) for various ϕ, A_{true}, and λ_z.

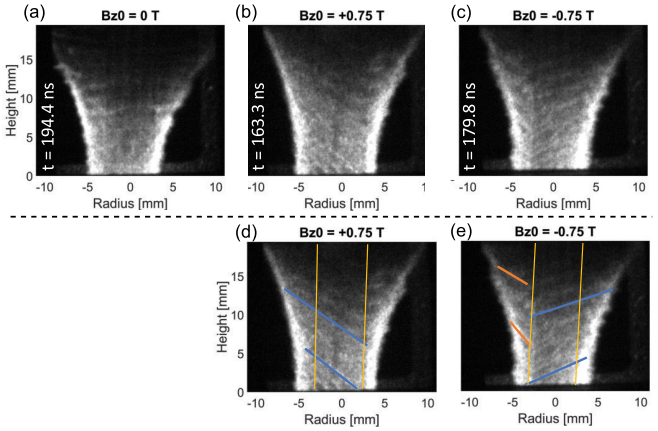

Fig. 6. Visible-light self-emission images taken as the imploding plasma sheath approaches the central rod for three different cases. (a) $B_{z0} = 0$. (b) $B_{z0} = +0.75$ T (at $z = 10$ mm). (c) $B_{z0} = -0.75$ T (at $z = 10$ mm). With $B_{z0} > 0$, the helical instability structure is left handed relative to the z-axis. With $B_{z0} < 0$, the helical instability structure is right handed relative to the z-axis. (d) and (e) Examples of the striation tracing. Striations traced along the front surface are marked in blue. Striations traced along the back surface are marked in orange. The left and right edges of the rod are marked in yellow.

From Fig. 6, the orientation of the striations indicates that the $B_{z0} = 0$ case produced $m = 0$ structure (horizontal striations), while the two $B_{z0} \neq 0$ cases produced $m \geq 1$ structure (diagonal striations). Note that both the front and back sides of the plasma shell are observable to the fast-framing camera in regions where the view of the back side is not obstructed by the central rod, indicating that the plasma is optically thin to visible-light self-emission. This results in images with diagonal helical striations going in only one direction immediately in front of the rod and in two opposing directions (forming a cross-hatch pattern) in the image regions just to the left or right of the rod. We note that the cross-hatch patterns produced on MAIZE are similar to the cross-hatch patterns produced in penetrating radiography experiments with $B_{z0} \geq 7$ T on the Z facility [18], [19]. From the direction of the striations immediately in front of the rod, the handedness of the helical instability structure can be determined. With $B_{z0} > 0$, the helical instability structure is left handed relative to the z-axis. With $B_{z0} < 0$, the helical instability structure is right handed relative to the z-axis. In both cases, the handedness matches that of the global magnetic field.

The helical striations were traced manually to determine the pitch angles presented in Fig. 7. In this figure, four different shots are presented. Three of these shots used a copper rod, while one shot used a dielectric rod. Solid and dashed lines with the same color are from the same shot, but at two different times. The earlier times are from when the plasma near the bottom of the image is at a smaller radius than the plasma near the top of the image (i.e., while the zippering process along the rod is still in progress). The later times are from after the zippering process has completed. These data show how the pitch angles vary as a function of height. They also show how the pitch angles increase as the radii decrease. For example, for the $B_{z0} = -0.75$ T case at $z = 14$ mm and $t = 173$ ns, the measured plasma radius is $r \approx 7$ mm, and the measured pitch angle is around $20° \pm 3°$. By $t = 307$ ns, for this same height of $z = 14$ mm, the plasma has fully collapsed onto the central rod with an outer plasma radius of $r \approx 4$ mm, and the pitch angle has increased to nearly $40° \pm 4°$.

Increasing pitch angles with decreasing plasma radii is consistent with the phenomenon of pitch locking (or conservation of pitch) [18], [23]. With this phenomenon, since the pitch is constant, the pitch *angle* must increase to accommodate the decrease in the plasma radius as the sheath implodes. Throughout our imaging data, where the conical plasma sheath is observed, steeper pitch angles are present near the bottom of the imploding sheath, where the plasma radii are smaller [see Fig. 6(b)–(e)]. Thus, as the plasma sheath implodes, the helical striations (which are initially more horizontally oriented) begin to steepen. The steepening persists until the implosion stagnates on the central rod, at which point the steepening ceases, and the pitch angle remains constant. The constant pitch angle post stagnation onto the rod can be seen, for example, via the blue curves in Fig. 7(a), for $z = 2$–4 mm, where the bottom of the plasma has already fully stagnated onto the rod prior to the earlier frame time of 173 ns. Thus, comparing the earlier and later frame times, we see that the pitch angle remains relatively constant, measuring $35° \pm 3°$ at $t = 173$ ns and $34° \pm 4°$ at $t = 307$ ns. The observation

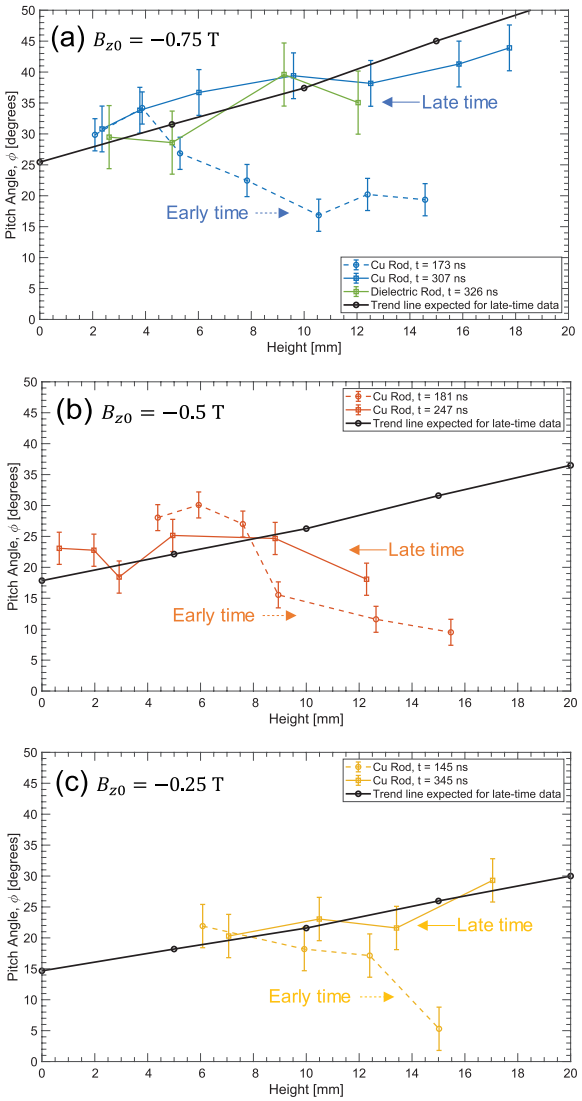

Fig. 7. Measured helical pitch angles along the height of the plasma at various times during the implosion for the three different applied axial magnetic field strengths tested. (a) $B_{z0} = -0.75$ T. (b) $B_{z0} = -0.5$ T. (c) $B_{z0} = -0.25$ T. Solid and dashed lines with the same color are from the same shot, but at two different times. The earlier times (dashed lines) are from when the plasma near the bottom of the imploding plasma sheath is at a smaller radius than the plasma near the top of the sheath (i.e., while the zippering process along the rod is still in progress). The later times (solid lines) are from after the zippering process has been completed. The green line in (a) represents the case where a dielectric rod was used instead of a copper rod. The black solid lines represent the scaling trends expected for the late-time (final) pitch angles when accounting for the axial variation in B_{z0}. Note that $B_{z0} = B_{z0}(z)$ because the fringe field (i.e., the field below the applied magnetic field coil) was used in these experiments.

of pitch locking raises the important question of when in the current pulse does the pitch become locked in? This is a question that we hope to study in the near future.

From the poststagnation (late-time) imaging data, the final pitch angles were larger for larger $|B_{z0}|$. Additionally, we observed larger increases in the final pitch angles over the higher field range of $|B_{z0}| = 0.5$–0.75 T than over the lower field range of $|B_{z0}| = 0.25$–0.5 T. For example, for the data points closest to $z = 10$ mm, the final pitch angles for $|B_{z0}| = 0.25$, 0.5, and 0.75 T were $23° \pm 4°$, $25° \pm 3°$, and $39° \pm 4°$, respectively.

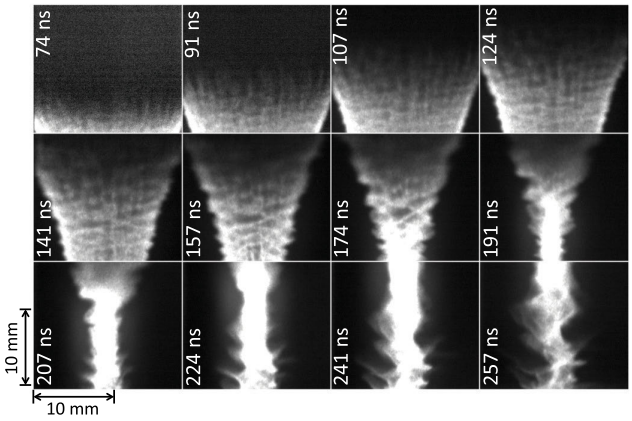

Fig. 8. Visible-light self-emission images of an argon gas-puff z-pinch imploding without a central rod. The axial magnetic field value applied was $B_{z0} = +0.5$ T. Note the simultaneous presence of both vertical filaments and helical striations. The vertical filaments are present only in shots with B_{z0} applied.

Because our preapplied axial field was a fringe field and thus a function of axial position [i.e., $B_{z0} = B_{z0}(z)$], the final pitch angles (i.e., the pitch angles persisting poststagnation onto the central rod) were also a function of z. This is illustrated in Fig. 7, where the black solid lines represent the scaling trends expected for the final (late-time) pitch angles when accounting for the axial variation in B_{z0}. These trend lines (black solid lines) fit the late-time data (solid colored lines) reasonably well for the $B_{z0} = -0.25$ T and -0.75 T cases, while the agreement is marginal for the $B_{z0} = -0.5$ T case. Note that the early-time experimental data (dashed lines) is not expected to agree with the late-time trend lines (black solid lines) because the early-time data is still in the process of zippering, with an implosion radius that varies with axial position, whereas the late-time trend lines assume that all of the plasma has collapsed onto the rod and thus the plasma radius does not vary with axial position.

Our experiments with a dielectric rod [green solid line in Fig. 7(a)] also produced large helical pitch angles, similar to those that formed when using the copper rod. This is interesting because flux compression to the copper rod should amplify the applied axial field more than in the case of the dielectric rod, since the field can slip through to the axis in the case of the dielectric rod. This may be evidence to suggest that the pitch of these helical structures is locked in and conserved very early in the current pulse, when the magnitudes of B_z and B_θ are similar.

In Fig. 8, we present visible-light self-emission images of an argon gas-puff z-pinch imploding without a center rod, which allows the implosion to stagnate on axis. The images taken prior to stagnation clearly show the steep crosshatch pattern of the helical modes, since the back side of the plasma shell is now fully visible (i.e., it is no longer obstructed by a central rod). An interesting observation here is that vertical filaments appear early in time and persist throughout the implosion (simultaneously with the helical striations), but these vertical filaments only appear in cases where an axial magnetic field is applied (in this case, $B_{z0} = +0.5$ T). Presumably, the bright structures shown in the images represent regions of high

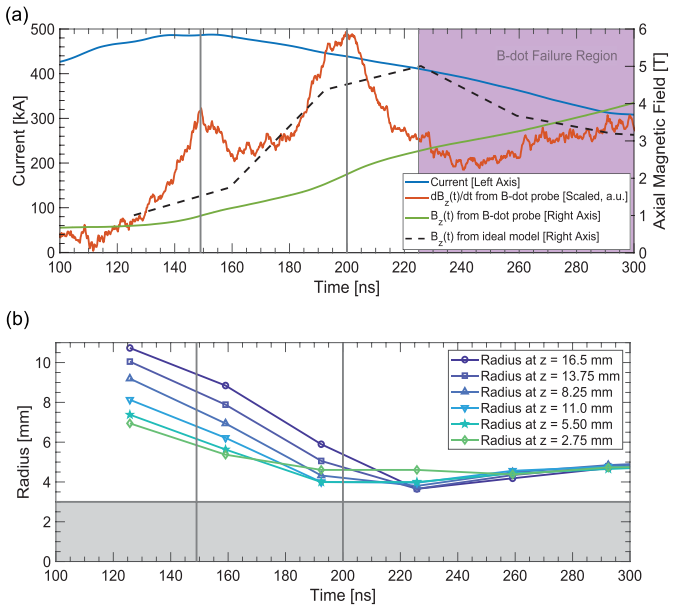

Fig. 9. (a) Magnetic flux compression measurements on shot 3151. Plotted is the MAIZE drive current (blue); the scaled dB_z/dt waveform measured by the B-dot probe (orange); the measured axial magnetic field, $B_z(t)$ (green); an ideal flux compression waveform (black dashed), calculated using $|B_{z0}| = 0.75$ T and the measured plasma radius, $r(t)$, at $z = 10$ mm; and the probe failure region (purple shading). (b) Plasma trajectories for the same shot at various axial locations. The gray shaded area represents the central rod. In both (a) and (b), the black vertical lines indicate times of peak dB/dt.

current density. One possible explanation for the vertical filamentation may be the axial magnetic field promoting vertical gas breakdown channels to the sharper parts of the metallic anode mesh. These fascinating phenomena and others will be the subjects of future studies.

D. Magnetic Flux Compression

Magnetic flux compression measurements are presented in Fig. 9. Here, the initial axial field was $B_{z0} = -0.75$ T at $z = 10$ mm. Additionally, a dielectric rod was used (instead of a metal rod) to house a B-dot probe and enable $B_z(t)$ measurements on axis. At peak compression ($t = 225$ ns), the B-dot probe measured an axial field strength of $B_z(t) = -2.6 \pm 0.5$ T.

The ideal flux compression curve in Fig. 9 comes from a model where all of the axial magnetic flux is conserved inside of an imploding thin shell—i.e., the thin shell is assumed to have zero resistivity. The evolution of the axial magnetic field is then calculated using

$$B_{z,\text{ideal}}(t) = B_{z0}\left[\frac{r_0}{r(t)}\right]^2, \tag{2}$$

where $r_0 = 10$ mm is the initial radius of the thin shell and $r(t)$ is the radius of the thin shell during the implosion. The $r(t)$ values are taken from the visible-light self-emission images at $z = 10$ mm.

From Fig. 9, we see that the measured $B_z(t)$ waveform is approximately 50% of the ideal flux compression waveform. The overestimate of the ideal model is at least partially due to the fact that the real plasma shell has finite resistivity. This allows $B_z(t)$ to diffuse through the shell wall and leak out of the compressed plasma regions. Another possible explanation is that plasma could have formed on the outer surface of the dielectric rod, due to either precursor plasma accumulating on the rod or dielectric breakdown occurring over the surface of the rod. Plasma along the surface of the rod could then shield the B-dot probe inside the rod from the compressed axial field outside the rod. (Note that by "precursor plasma," we mean a low-density plasma that fills the region of space between the outer surface of the dielectric rod and the inner surface of the imploding plasma sheath.)

In Fig. 9, the dB/dt curve has two observable peaks. The first peak occurs when the imploding plasma shell is still in flight, at a radius of 5.5–9.5 mm. Thus, it is possible that this first peak is due to a shock wave being launched ahead of the imploding plasma sheath into a precursor plasma, where $B_z(t)$ is frozen into this precursor plasma. We note that similar phenomena were observed in [37]. The second peak occurs at the point where all of the plasma has been compressed onto the rod. We note that just after peak compression, the dB/dt signal hangs on a nearly constant positive value and does not return to zero for a very long time (~800 ns). This is much longer than the driving current pulse on MAIZE. It is suspected that the probe has thus failed as a result of the implosion compressing the probe on the axis and/or a stream of plasma bombarding the signal cable above the anode mesh. Another possible explanation is that the flux in the B-dot probe simply continues to increase due to the diffusion of the axial field from the plasma volume into the hollow dielectric rod. This may be possible as the plasma persists beyond $t = 600$ ns. Simulations could help resolve these questions, as could additional dB/dt measurements, preferably with differential B-dot probes instead of single-ended B-dot probes.

IV. Conclusion

The experimental results presented in this article have demonstrated a newly developed platform to study instability development and magnetic flux compression in a low-density plasma as the plasma implodes onto a dense cylindrical target. Two configurations were examined, one with a copper central rod and the other with a dielectric central rod, both of which were used in conjunction with an argon gas shell. The trajectory of the imploding plasma shell was characterized for this configuration, and it was found that the plasma fully compressed onto the center rod over a time range of $t = 194$–260 ns, due to a zippering effect. Even though zippering occurred, the final compression of the plasma was relatively uniform over the surface of the central rod. The results of this characterization will be useful for future experiments related to gas on metallic liner dynamics.

Well-defined helical instabilities with large pitch angles were observed when the load region was premagnetized with an axial field of $|B_{z0}| = 0.25$–0.75 T (at $z = 10$ mm). The direction of the helices is determined by the polarity of the applied axial field. With $B_{z0} > 0$, the helices are left handed. With $B_{z0} < 0$, the helices are right handed. In both cases, the handedness matches that of the global magnetic field.

The pitch angles were found to be significantly larger in the $|B_{z0}| = 0.75$ T case than in the $|B_{z0}| \leq 0.5$ T cases. This might indicate a discontinuous jump to a higher azimuthal mode number in the $|B_{z0}| = 0.75$ T case, similar to what has been reported in previous studies [23]. The final pitch angle obtained (after full compression of the plasma onto the central rod) seems to trend with $|B_{z0}|$. The results show evidence of pitch locking early in the current pulse.

Magnetic flux compression measurements, taken on axis using a B-dot probe housed inside a dielectric central rod, returned two interesting results. The first result is the observation of two peaks in the dB/dt curve, the origins of which are still in question. A potential answer is that the first peak is due to a shock wave being launched ahead of the imploding plasma sheath into a precursor plasma, where $B_z(t)$ is frozen into this precursor plasma. The second peak occurs at the point where all of the plasma has been compressed onto the rod. The second result is that the measured flux compression is about 50% efficient relative to an ideal flux compression model, so about half of the flux (or field) escapes the imploding plasma sheath. However, the ideal model assumes that the imploding plasma is an infinitely thin shell with zero resistivity, when in fact it is a sheath with some finite thickness and finite resistivity. Measurement of the axial magnetic field distribution within the sheath is critical to understand the amount of flux compression that occurs. In general, numerical simulations and further experimentation will be needed to fully understand the observations reported in this article. These efforts will be the subjects of future studies.

ACKNOWLEDGMENT

Sandia National Laboratories is a multimission laboratory managed and operated by National Technology and Engineering Solutions of Sandia, LLC (NTESS), a wholly owned subsidiary of Honeywell International Inc., for the U.S. Department of Energy's National Nuclear Security Administration (DOE/NNSA) under Contract DE-NA0003525. This written work is co-authored by an employee of NTESS. The employee, not NTESS, owns the right, title, and interest in and to the written work and is responsible for its contents. Any subjective views or opinions that might be expressed in the written work do not necessarily represent the views of the U.S. Government. The publisher acknowledges that the U.S. Government retains a nonexclusive, paid-up, irrevocable, worldwide license to publish or reproduce the published form of this written work or allow others to do so, for U.S. Government purposes. The DOE will provide public access to results of federally sponsored research in accordance with the DOE Public Access Plan.

REFERENCES

[1] E. G. Harris, "Rayleigh-Taylor instabilities of a collapsing cylindrical shell in a magnetic field," *Phys. Fluids*, vol. 5, no. 9, pp. 1057–1062, Sep. 1962. [Online]. Available: https://aip.scitation.org/doi/abs/10.1063/1.1724473

[2] E. Ott, "Nonlinear evolution of the Rayleigh–Taylor instability of a thin layer," *Phys. Rev. Lett.*, vol. 29, no. 21, pp. 1429–1432, Nov. 1972, doi: 10.1103/PhysRevLett.29.1429.

[3] D. D. Ryutov, M. S. Derzon, and M. K. Matzen, "The physics of fast Z pinches," *Rev. Mod. Phys.*, vol. 72, pp. 167–223, Jan. 2000, doi: 10.1103/RevModPhys.72.167.

[4] R. E. Reinovsky et al., "Instability growth in magnetically imploded high-conductivity cylindrical liners with material strength," *IEEE Trans. Plasma Sci.*, vol. 30, no. 5, pp. 1764–1776, Oct. 2002.

[5] A. R. Miles, "Nonlinear Rayleigh–Taylor instabilities in fast Z pinches," *Phys. Plasmas*, vol. 16, no. 3, Mar. 2009, Art. no. 032702, doi: 10.1063/1.3088020.

[6] Y. Y. Lau, J. C. Zier, I. M. Rittersdorf, M. R. Weis, and R. M. Gilgenbach, "Anisotropy and feedthrough in magneto-Rayleigh–Taylor instability," *Phys. Rev. E, Stat. Phys. Plasmas Fluids Relat. Interdiscip. Top.*, vol. 83, no. 6, Jun. 2011, Art. no. 066405.

[7] P. Zhang et al., "Effects of magnetic shear on magneto-Rayleigh–Taylor instability," *Phys. Plasmas*, vol. 19, no. 2, Feb. 2012, Art. no. 022703, doi: 10.1063/1.3680646.

[8] A. L. Velikovich and P. F. Schmit, "Bell-Plesset effects in Rayleigh–Taylor instability of finite-thickness spherical and cylindrical shells," *Phys. Plasmas*, vol. 22, no. 12, Dec. 2015, Art. no. 122711, doi: 10.1063/1.4938272.

[9] D. A. Yager-Elorriaga, P. Zhang, A. M. Steiner, N. M. Jordan, Y. Y. Lau, and R. M. Gilgenbach, "Seeded and unseeded helical modes in magnetized, non-imploding cylindrical liner-plasmas," *Phys. Plasmas*, vol. 23, no. 10, Oct. 2016, Art. no. 101205, doi: 10.1063/1.4965240.

[10] S. A. Slutz et al., "Pulsed-power-driven cylindrical liner implosions of laser preheated fuel magnetized with an axial field," *Phys. Plasmas*, vol. 17, no. 5, May 2010, Art. no. 056303, doi: 10.1063/1.3333505.

[11] M. R. Gomez et al., "Experimental demonstration of fusion-relevant conditions in magnetized liner inertial fusion," *Phys. Rev. Lett.*, vol. 113, no. 15, Oct. 2014, Art. no. 155003.

[12] M. R. Gomez et al., "Performance scaling in magnetized liner inertial fusion experiments," *Phys. Rev. Lett.*, vol. 125, Oct. 2020, Art. no. 155002, doi: 10.1103/PhysRevLett.125.155002.

[13] D. B. Sinars et al., "Review of pulsed power-driven high energy density physics research on Z at Sandia," *Phys. Plasmas*, vol. 27, no. 7, Jul. 2020, Art. no. 070501, doi: 10.1063/5.0007476.

[14] D. A. Yager-Elorriaga et al., "An overview of magneto-inertial fusion on the Z machine at Sandia National Laboratories," *Nucl. Fusion*, vol. 62, no. 4, Feb. 2022, Art. no. 042015, doi: 10.1088/1741-4326/ac2dbe.

[15] D. C. Rovang et al., "Pulsed-coil magnet systems for applying uniform 10–30 T fields to centimeter-scale targets on Sandia's Z facility," *Rev. Sci. Instrum.*, vol. 85, no. 12, Dec. 2014, Art. no. 124701, doi: 10.1063/1.4902566.

[16] R. D. McBride et al., "Penetrating radiography of imploding and stagnating beryllium liners on the Z accelerator," *Phys. Rev. Lett.*, vol. 109, no. 13, Sep. 2012, Art. no. 135004.

[17] R. D. McBride et al., "Beryllium liner implosion experiments on the Z accelerator in preparation for magnetized liner inertial fusion," *Phys. Plasmas*, vol. 20, no. 5, May 2013, Art. no. 056309.

[18] T. J. Awe et al., "Observations of modified three-dimensional instability structure for imploding Z-pinch liners that are premagnetized with an axial field," *Phys. Rev. Lett.*, vol. 111, no. 23, Dec. 2013, Art. no. 235005.

[19] T. J. Awe et al., "Modified helix-like instability structure on imploding Z-pinch liners that are pre-imposed with a uniform axial magnetic field," *Phys. Plasmas*, vol. 21, no. 5, Apr. 2014, Art. no. 056303, doi: 10.1063/1.4872331.

[20] D. Mikitchuk et al., "Mitigation of instabilities in a Z-pinch plasma by a preembedded axial magnetic field," *IEEE Trans. Plasma Sci.*, vol. 42, no. 10, pp. 2524–2525, Oct. 2014. https://ieeexplore.ieee.org/document/6835195

[21] E. S. Lavine et al., "Implosion dynamics of triple-nozzle gas-puff Z pinches on COBRA," *Phys. Plasmas*, vol. 28, no. 2, Feb. 2021, Art. no. 022703, doi: 10.1063/5.0030936.

[22] L. Atoyan et al., "Helical plasma striations in liners in the presence of an external axial magnetic field," *Phys. Plasmas*, vol. 23, no. 2, Feb. 2016, Art. no. 022708, doi: 10.1063/1.4942787.

[23] D. A. Yager-Elorriaga et al., "Discrete helical modes in imploding and exploding cylindrical, magnetized liners," *Phys. Plasmas*, vol. 23, no. 12, Dec. 2016, Art. no. 124502, doi: 10.1063/1.4969082.

[24] D. A. Yager-Elorriaga et al., "Evolution of sausage and helical modes in magnetized thin-foil cylindrical liners driven by a Z-pinch," *Phys. Plasmas*, vol. 25, no. 5, Mar. 2018, Art. no. 056307, doi: 10.1063/1.5017849.

[25] E. P. Yu et al., "Seeding the electrothermal instability through a three-dimensional, nonlinear perturbation," *Phys. Rev. Lett.*, vol. 130, no. 25, Jun. 2023, Art. no. 255101, doi: 10.1103/PhysRevLett.130.255101.

[26] J. M. Woolstrum, C. E. Seyler, and R. D. McBride, "Hall instability driven seeding of helical magneto-Rayleigh–Taylor instabilities in axially premagnetized thin-foil liner Z-pinch implosions," *Phys. Plasmas*, vol. 29, no. 12, Dec. 2022, Art. no. 122701, doi: 10.1063/5.0103651.
[27] J. M. Woolstrum, D. E. Ruiz, N. D. Hamlin, K. Beckwith, and M. R. Martin, "Hall interchange instability as a seed for helical magneto-Rayleigh–Taylor instabilities in magnetized liner inertial fusion Z-pinches scaled from Z-machine parameters to a next generation pulsed power facility," *Phys. Plasmas*, vol. 30, no. 7, Jul. 2023, Art. no. 072712, doi: 10.1063/5.0156806.
[28] D. D. Ryutov et al., "Effect of axial magnetic flux compression on the magnetic Rayleigh–Taylor instability (theory)," *AIP Conf. Proc.*, vol. 1639, no. 1, pp. 63–66, Dec. 2014, doi: 10.1063/1.4904778.
[29] N. Bennett et al., "Electrode plasma formation and melt in Z-pinch accelerators," *Phys. Rev. Accel. Beams*, vol. 26, no. 4, Apr. 2023, Art. no. 040401, doi: 10.1103/PhysRevAccelBeams.26.040401.
[30] R. D. McBride et al., "A primer on pulsed power and linear transformer drivers for high energy density physics applications," *IEEE Trans. Plasma Sci.*, vol. 46, no. 11, pp. 3928–3967, Nov. 2018. [Online]. Available: https://ieeexplore.ieee.org/document/8526364
[31] T. J. Smith et al., "Additively manufactured electrodes for plasma and power-flow studies in high-power transmission lines on the 1-MA MAIZE facility," *Rev. Sci. Instrum.*, vol. 92, no. 5, May 2021, Art. no. 053550, doi: 10.1063/5.0043856.
[32] A. Shah, "Effects of pre-ionization on the gas-puff Z-pinch," Ph.D. dissertation, Dept. Appl. Phys., Univ. Michigan, Ann Arbor, MI, USA, 2022, doi: 10.7302/5927.
[33] A. P. Shah et al., "Development of a gas-puff Z-pinch for the MAIZE linear transformer driver," *IEEE Trans. Plasma Sci.*, vol. 52, 2024.
[34] D. A. Yager-Elorriaga, A. M. Steiner, S. G. Patel, N. M. Jordan, Y. Y. Lau, and R. M. Gilgenbach, "Technique for fabrication of ultrathin foils in cylindrical geometry for liner-plasma implosion experiments with sub-megaampere currents," *Rev. Sci. Instrum.*, vol. 86, no. 11, Nov. 2015, Art. no. 113506, doi: 10.1063/1.4935838.
[35] A. G. Rousskikh et al., "Effect of the axial magnetic field on a metallic gas-puff pinch implosion," *Phys. Plasmas*, vol. 23, no. 6, Jun. 2016, Art. no. 063502, doi: 10.1063/1.4953048.
[36] P. C. Campbell, "Stability and power coupling in dynamic screw pinch plasmas," Ph.D. dissertation, Dept. Nucl. Eng. Radiological Sci., Univ. Michigan, Ann Arbor, MI, USA, 2020, doi: 10.7302/27.
[37] P. C. Campbell et al., "Liner implosion experiments driven by a dynamic screw pinch," *Phys. Plasmas*, vol. 28, no. 8, Aug. 2021, Art. no. 082707, doi: 10.1063/5.0044906.

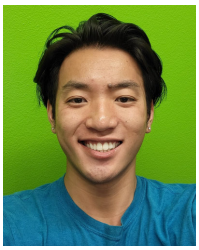

Joe M. Chen (Member, IEEE) received the B.S. and M.S.E. degrees in electrical engineering from the University of New Mexico, Albuquerque, NM, USA, in 2018 and 2021, respectively, with a focus on applied electromagnetics. He is currently pursuing the Ph.D. degree in nuclear engineering and radiological sciences with the University of Michigan, Ann Arbor, MI, USA, with a focus on plasma physics. His thesis studies are on magneto Rayleigh–Taylor instability and energy dynamics on z-pinch configured implosions.

George V. Dowhan (Member, IEEE) received the B.S. degree in applied physics from the Rensselaer Polytechnic Institute, Troy, NY, USA, in 2018, with a focus on medical physics, and the M.S.E. degree in nuclear engineering and radiological sciences and the Ph.D. degree in applied physics from the University of Michigan, Ann Arbor, MI, USA, in 2021 and 2023, respectively. His thesis was on current delivery to high energy density (HED) micropinch plasmas and the dynamics of X-pinches.

Brendan J. Sporer received the dual B.S. degrees in nuclear and mechanical engineering from the Pennsylvania State University, State College, PA, USA, in 2017, and the Ph.D. degree in nuclear engineering and radiological sciences from the University of Michigan, Ann Arbor, MI, USA, in 2023. His thesis was on plasma physics, pulsed-power, and high-energy-density magneto-inertial fusion.

He is currently a Scientist with TAE Technologies, Foothill Ranch, CA, USA, a private company pursuing magnetic fusion energy based on the neutral beam-driven field-reversed configuration.

David A. Yager-Elorriaga (Member, IEEE) received the B.A. degree in physics and mathematics with a minor in Spanish from the Gettysburg College, Gettysburg, PA, USA, in 2010, and the M.S.E. and Ph.D. degrees in nuclear engineering and radiological sciences from the University of Michigan, Ann Arbor, MI, USA, in 2013 and 2017, respectively.

Since 2017, he has been a Staff Member with Sandia National Laboratories, Albuquerque, NM, USA, where he focuses on inertial confinement fusion and high-energy-density physics on the Z machine.

Dr. Yager-Elorriaga received the National Science Foundation Graduate Fellowship in 2012 to investigate magneto Rayleigh–Taylor instability in z-pinches.

Nicholas M. Jordan (Senior Member, IEEE) received the B.S.E., M.S.E., and Ph.D. degrees in nuclear engineering and radiological sciences from the University of Michigan, Ann Arbor, MI, USA, in 2002, 2004, and 2008, respectively.

From 2008 to 2013, he was with Cybernet Systems, Ann Arbor, where he developed technology to disable uncooperative vehicles using microwave pulses. He is currently an Associate Research Professor with the Plasma, Pulsed Power, and Microwave Laboratory, University of Michigan. His current research interests include pulsed power, z-pinch physics, plasma discharges, magnetrons, magnetically insulated line oscillators (MILOs), crossed-field amplifiers (CFAs), and other high-power microwave devices.

Ryan D. McBride (Member, IEEE) received the M.S. and Ph.D. degrees in electrical engineering from Cornell University, Ithaca, NY, USA, in 2007 and 2009, respectively.

From 2008 to 2016, he was with Sandia National Laboratories, Albuquerque, NM, USA, where he held appointments as a Staff Physicist and a Department Manager. At Sandia, he conducted research in nuclear fusion, high-power radiation sources, and high-pressure material properties using the 30-MA Z facility. He is currently a Professor of nuclear engineering and radiological sciences at the University of Michigan (UM), Ann Arbor, MI, USA. He specializes in plasma physics, high-energy-density physics, nuclear fusion, high-power radiation sources, and pulsed-power technology. Since 2021, he has served as the Director of UM's Plasma, Pulsed Power, and Microwave Laboratory, which is home to the MAIZE and BLUE linear transformer driver facilities.